An Investigation of the Crystal Structure and Ionic Pathways of the Hexagonal Perovskite Derivative $Ba_{3-x}VMoO_{8.5-x}$

Dylan N. Tawse [a], Asma Gilane [a, b], Sacha Fop [a, c], Alfonso Martinez-Felipe [d], Falak Sher [b], Ronald I. Smith [c] and Abbie C. Mclaughlin*[a]

[a] Department of Chemistry, University of Aberdeen, Meston Walk, Aberdeen AB24 3UE, United Kingdom

[b] Department of Chemistry and Chemical Engineering, SBA School of Science and Engineering, Lahore University of Management Sciences (LUMS), Lahore, Pakistan

[c] ISIS Facility, Rutherford Appleton Laboratory, Harwell Campus, Didcot OX11 0QX, United Kingdom

[d] Chemical and Materials Engineering Group, School of Engineering, University of Aberdeen, King's College, Old Aberdeen, AB24 3UE, UK

* a.c.mclaughlin@abdn.ac.uk

Abstract

The hexagonal perovskite derivatives $Ba_3NbMoO_{8.5}$, $Ba_3NbWO_{8.5}$ and $Ba_3VWO_{8.5}$ have recently been reported to exhibit significant oxide ion conductivity. Here we report the synthesis and crystal structure of the hexagonal perovskite derivative $Ba_{3-x}VMoO_{8.5-x}$. Rietveld refinement from neutron and X-ray diffraction data show that the cation vacancies are ordered on the M2 site leading to a structure consisting of palmierite-like layers of $M1O_x$ polyhedra separated by vacant octahedral layers. In contrast to other members of the $Ba_3M'M''O_{8.5}$ family, $Ba_{3-x}VMoO_{8.5-x}$ is not stoichiometric and both barium and oxygen vacancies are present. Although synthesised in air at elevated temperatures, $Ba_{3-x}VMoO_{8.5-x}$ is unstable at lower temperatures, as illustrated by the formation of $BaCO_3$ and $BaMoO_4$ by heat treatment in air at 400 °C. This precludes measurement of the electrical properties. However, bond-valence site energy (BVSE) calculations strongly suggest that oxide ion conductivity is present in $Ba_{3-x}VMoO_{8.5-x}$.

Introduction

Research into oxide ion conductors has recently increased due to their use as electrolytes for solid oxide fuel cells (SOFC) and solid oxide electrolyser cells (SOEC), oxygen separation membranes, oxygen sensors and oxygen pumps [1–5]. Currently, SOFCs require high temperatures (> 700 °C) to operate efficiently. These high operating temperatures lead to poor durability of components, increased costs, slow start up times and issues with selecting compatible materials [2,5]. There is a significant amount of research being carried out into developing oxide ion conductors that can operate at intermediate temperatures (400-600 °C). The oxide ion conductivity of a material is linked to the crystal structure and is usually enabled by the presence of oxygen vacancies and disorder [1,6].

Numerous crystal systems including fluorite and $La_2Mo_2O_9$ (LAMOX) systems, silicon and germanium apatites and Bi-based compounds (such as BIMEVOX and BICUVOX) have displayed fast oxide ionic conductivity [7–11]. Oxide ionic conductivity has also been seen for a number of cubic perovskites including doped lanthanum gallates (such as LSGM) and sodium bismuth titanate (NBT) [12–15].

Significant oxide ion conductivity has recently been reported in the hexagonal perovskite derivative $Ba_3NbMoO_{8.5}$, with a bulk ionic conductivity of 2.2×10^{-3} S cm^{-1} of at 600 °C [16]. $Ba_3NbMoO_{8.5}$ crystallises in a hybrid structure between that of the 9R perovskite polytype and palmierite structures. The 9R hexagonal perovskite polytype ($A_3B_3O_9$) is described by the stacking along the *c* ais of nine BaO_3 layers with the stacking sequence $(hhc)_3$. Trimers of face sharing MO_6 octahedra are connected *via* corner sharing. The palmierite ($A_3B_2O_8$) structure also displays the $(hhc)_3$ stacking sequence and forms as a result of oxygen deficient BaO_2 layers resulting in isolated MO_4 tetrahedra followed by octahedral vacancies [17]. The hybrid structure displayed by $Ba_3NbMoO_{8.5}$ contains cationic vacancies distributed across the two metal sites, M1 and M2. Partial occupation of two distinct crystallographic oxygen positions, O2 and O3, leads to variable coordination $M1O_x$ polyhedra with the occupation of O2 producing $M1O_6$ octahedra and O3 producing $M1O_4$ tetrahedra [16]. Investigation into the local structure has shown that the presence of positional disorder leads to intermediate 5-fold geometries between that of the $M1O_6$ and $M1O_4$ polyhedra [18,19].

$Ba_3NbMoO_{8.5}$ displays solid oxide ion conductivity over a wide range of pO_2 values (10^{-20} to 1 atm) and is highly stable under both reducing and oxidising conditions at 600 °C [16]. An investigation into the effect of temperature on the average structure of $Ba_3NbMoO_{8.5}$ concluded that a structural rearrangement occurs in which the relative average occupancies of the O2/O3 sites changes as temperature increases [20]. There is a notable increase in the O3 occupation with a simultaneous decrease in O2 occupation above 300 °C so that there is a preference for lower coordination environments for the M1 site upon increasing the temperature. This is further supported by pair distribution function (PDF) data which showed that although the 5-fold coordination is prevalent on a

local scale, an increase in the number of local $M1O_4$ polyhedra is observed at elevated temperatures alongside a decrease in the number of local $M1O_6$ polyhedra [19]. This increase in lower coordination environments produces more low energy pathways for the diffusion of oxide ions resulting in an increase in oxide ion conductivity [20].

In corroboration, it has been shown that substitution with cations that are known to favour lower coordination geometries, such as V^{5+}, which favours tetrahedral geometry, can enhance the ionic conductivity [21,22]. Substitution of V^{5+} for Nb^{5+} to form the $Ba_3Nb_{1-x}V_xMoO_{8.5}$ series resulted in an increase in the bulk ionic conductivity by nearly one order of magnitude to 1.01 x 10^{-2} S cm^{-1} at 600 °C when x = 0.1 [22]. In contrast, substitution of Mo^{6+} by cations such as W^{6+}, which prefers octahedral geometry, show an increase in the occupation of the O2 site and reduced bulk conductivities. $Ba_3NbWO_{8.5}$ exhibits a bulk conductivity of approximately one order of magnitude lower than $Ba_3NbMoO_{8.5}$ at 450 °C [23,24]. Several investigations including neutron, synchrotron and PDF studies have confirmed that there is also a structural rearrangement in $Ba_3NbWO_{8.5}$ upon increasing the temperature so that the concentration of tetrahedra within the palmierite-like layer increases upon heating, similar to that observed in $Ba_3NbMoO_{8.5}$ [23,25].

We recently reported that the hexagonal perovskite derivative $Ba_7Nb_4MoO_{20}$ displays both high proton and oxide ion conductivity. $Ba_7Nb_4MoO_{20}$ is a 7H hexagonal perovskite derivative composed of an intergrowth of 12R hexagonal perovskite and palmierite-like layers, with similar structural features to $Ba_3NbMoO_{8.5}$. $Ba_7Nb_4MoO_{20}$ exhibits a bulk ionic conductivity of ~1.00 x 10^{-3} S cm^{-1} at 400 °C under dry conditions with an increase to ~3.16 x 10^{-3} S cm^{-1} when exposed to wet conditions at the same temperature [26]. This increase in conductivity is evidence of the high protonic conductivity exhibited by $Ba_7Nb_4MoO_{20}$ and is comparable to leading proton conductors. The synthesis and investigation of further hexagonal perovskite derivatives is therefore clearly warranted.

In this study, the synthesis, crystal structure and stability of $Ba_{3-x}VMoO_{8.5-x}$is reported with conduction pathways analysed through bond-valence site energy (BVSE) analysis. Structural refinement using X-ray and neutron diffraction data show that $Ba_{3-x}VMoO_{8.5-x}$ displays the same crystal structure as $Ba_3VWO_{8.5}$ with ordering of the cationic vacancies on the M2 sites [27]. BVSE calculations show that the ordering of cation vacancies hinders long-range diffusion of oxide ions parallel to the *c*-axis. However low energy diffusion pathways of the oxide ions along the palmierite layers are present which suggests that $Ba_{3-x}VMoO_{8.5-x}$ is also an oxide ion conductor.

Experimental

$Ba_{3-x}VMoO_{8.5-x}$ was prepared by solid-state reaction of stoichiometric amounts of $Ba(OH)_2$ (~95%, Aldrich), V_2O_5 (≥99.6%, Aldrich) and MoO_3 (99.5+%, Aldrich). No excess $Ba(OH)_2$ was added. The

starting materials were ground, pressed into a 13 mm pellet and transferred to an alumina crucible to be calcined at 900 °C for 10 hours. The pellet was then reground, pelleted and heated at 1200 °C for 48 hours before cooling to room temperature at 5 °C min^{-1}. The latter step was repeated until a phase pure compound was obtained.

X-ray powder diffraction data were collected at room temperature using a PANalytical Empyrean diffractometer equipped with a Cu Kα tube and a Johansson monochromator. Data were collected in the range 5 ° < 2θ < 120 ° with a step size of 0.013 °. Time-of-flight (TOF) neutron powder diffraction data were collected at room temperature on the Polaris diffractometer at the ISIS pulsed neutron source (Rutherford Appleton Laboratory, Harwell, Oxford, UK). A 5 g sample of $Ba_{3-x}VMoO_{8.5-x}$ was loaded into a cylindrical vanadium can of 8 mm diameter with data recorded from all five detector banks for a total of 350 μA h proton charge to the ISIS target, corresponding to ~2 hours exposure in the neutron beam. Rietveld refinements were performed on data from banks 2-5 using the GSAS/EXPGUI package [28,29]. As vanadium nuclei do not scatter neutrons strongly, an initial Rietveld refinement using high resolution X-ray diffraction data was performed [30].

The PIEFACE software package was used to perform the minimum bounding ellipsoid fitting to evaluate the distortion of the average metal coordination polyhedra as a result of substituting V^{5+} for Nb^{5+} [31]. The standard deviation, σ(*R*), of the three principal ellipsoid radii, where $R1 \geq R2 \geq R3$, was used to quantify the polyhedral distortion of the system.

Bond-valence site energy (BVSE) calculations were carried out using the *soft*BV program using the structural models produced from the Rietveld refinements [32,33]. The unit cell of the structural model was split into a dense grid of points with a resolution of 0.1 Å to ensure special positions of the crystal structure were included before BVSE landscapes for the interaction of a probe O^{2-} ion were calculated [32]. Diffusion pathways were determined with regions of low BVSE by direct visualisation of the connectivity of the isosurfaces and by examination of the calculated pathway segments. BVSE maps displaying two-dimensional diffusion pathways and saddle points were visualised using *VESTA* [34] while BVSE models of migration barriers were plotted from the energy profiles of the diffusion pathways.

Results and Discussion

The X-ray diffraction pattern of $Ba_{3-x}VMoO_{8.5-x}$ is shown in Fig. 1. The sample is phase pure and could be indexed with the space group $R\bar{3}m$ *H* (*a* = 5.86811(2) Å; *c* = 21.30104(9) Å) as reported for other members of the $Ba_3M'M''O_{8.5}$ family [16,23,27].

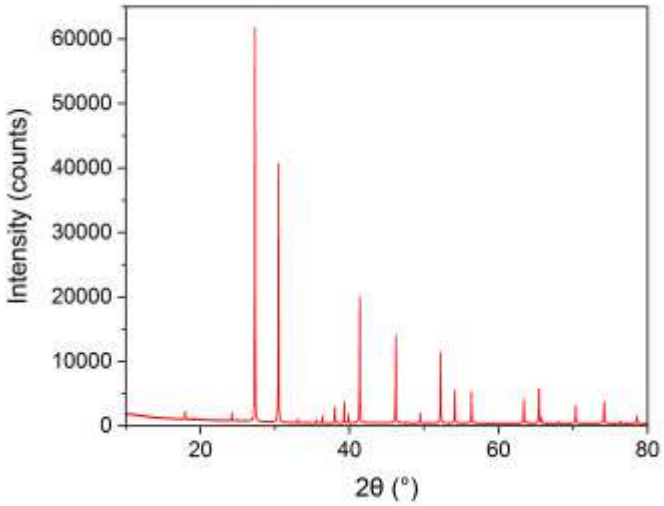

Figure 1. X-ray diffraction pattern of the as-prepared sample of $Ba_{3-x}VMoO_{8.5-x}$. The pattern can be indexed with the $R\bar{3}m$ *H* space group.

Samples of $Ba_{3-x}VMoO_{8.5-x}$ were annealed at 400 °C to 700 °C in 100 °C steps for 10 hours under air in addition to annealing at 300 °C and 400 °C in O_2. X-ray diffraction patterns were collected post annealing to investigate phase stability. Bragg reflections consistent with those of $BaCO_3$ were detected after exposure to air between 400 °C and 600 °C with $BaMoO_4$ impurity peaks displayed at 600 and 700 °C (Fig. 2a). At 600 °C weight fractions of ~ 5% $BaCO_3$ and ~ 3% $BaMoO_4$ are present within the sample. The $BaMoO_4$ impurity phase was also evident when a fresh sample was exposed to O_2 above 300 °C (Fig. 2b). $Ba_{3-x}VMoO_{8.5-x}$ forms impurities at a much lower temperature than $Ba_3NbMoO_{8.5}$, which sees the formation of the same $BaMoO_4$ impurity phase alongside $Ba_7Nb_4MoO_{20}$ in air above 650 °C [16]. The stability of $Ba_{3-x}VMoO_{8.5-x}$ is also considerably poorer than that of $Ba_3VWO_{8.5}$, which is stable in air at temperatures up to 900 °C [27]. This instability prevents the investigation of the electrical properties of $Ba_{3-x}VMoO_{8.5-x}$.

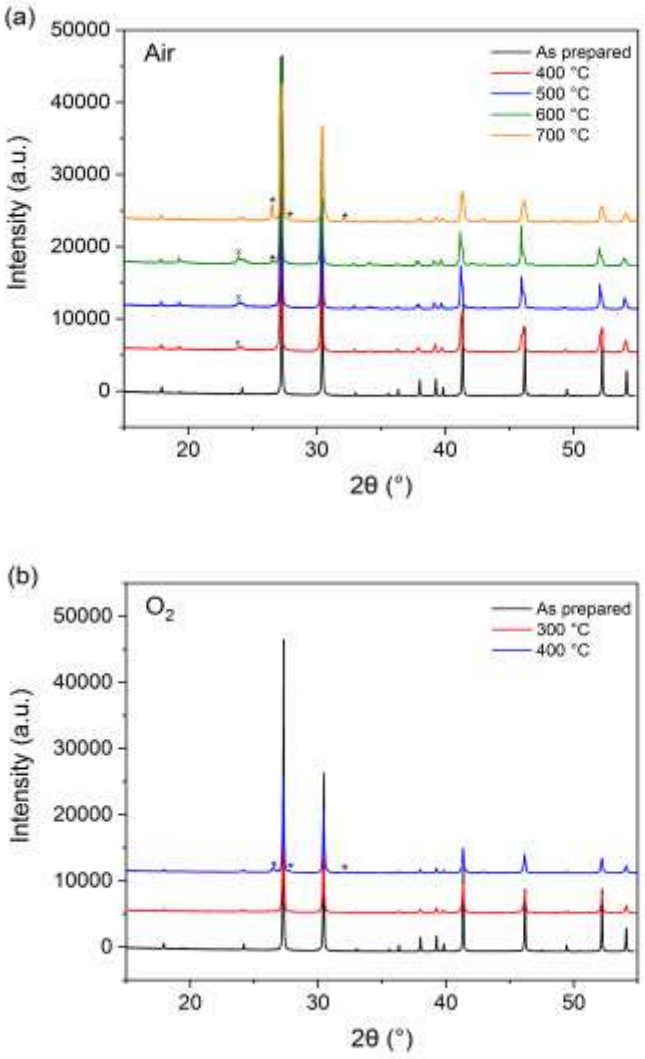

Figure 2. XRD patterns of $Ba_{3-x}VMoO_{8.5-x}$ after annealing for 10 hours in (a) air and (b) oxygen at selected temperatures. Asterisks and crosses represent peaks resulting from presence of $BaMoO_4$ and $BaCO_3$ impurities respectively.

As vanadium has a low scattering cross-section for neutrons, it was important to perform an initial Rietveld refinement on X-ray diffraction data to determine the fractional occupancies of V and Mo. The 9R perovskite and palmierite hybrid structure reported for other $Ba_3M'M''O_{8.5}$ compounds was used as a starting model. Oxygen atoms are found on three Wyckoff sites; 18*h* which is common to both the 9R and palmierite structures, 9*e* that is found in the 9R polytype perovskite and 6*c* that is found in the palmierite structure. The Ba atoms occupy two Wyckoff sites with Ba1 present on the 3*a* site and Ba2 on the 6*c* site. The transition metal atoms share the same positions in this model with M1 at the 6*c* position and M2 at the 3*b* position [16]. The refined model obtained from this initial refinement showed no significant evidence of the M2 site being occupied by either V^{5+} or Mo^{6+}. The

X-ray difference Fourier map also showed no significant missing scattering density on or around the M2 site. The V and Mo fractional occupancies at the M1 site were refined freely in the XRD refinement. They both refined to within ±1% of the full occupancy and were subsequently fixed at 0.5.

The cation order of $Ba_{3-x}VMoO_{8.5-x}$ is therefore the same as reported for $Ba_3VWO_{8.5}$. Unlike $Ba_3NbMoO_{8.5}$ and $Ba_3NbWO_{8.5}$, where the cationic vacancies are distributed across the M1 and M2 sites, the vacancies are ordered on the M2 site in both $Ba_3VWO_{8.5}$ and $Ba_{3-x}VMoO_{8.5-x}$ [16,23,27] (Fig. 3). The following statistical parameters were obtained; χ^2 = 3.838, R_p = 7.00 %, R_{wp} = 9.13 %, and a good match between the calculated and observed histograms was found (Fig. S1 and Table S1).

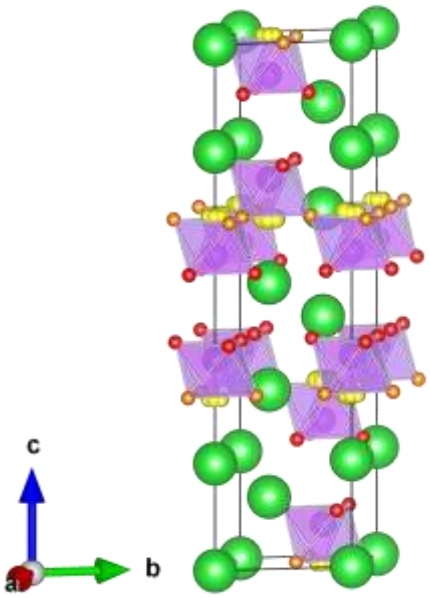

Figure 3. Crystal structure of $Ba_{3-x}VMoO_{8.5-x}$. Average hybrid structure composed of a combination of the 9R perovskite polytype and palmierite structures. Colours: green, Ba1/Ba2; purple, V1/Mo1; red, O1; orange, O2; and yellow, O3.

The resulting model from the X-ray refinement was then used as a starting model for the Rietveld refinement with time-of-flight neutron powder diffraction data. The atomic displacement parameters were modelled anisotropically for all metal atoms and O1. The O2 and O3 atoms were modelled isotropically. Due to the highly anisotropic thermal displacement parameters found for O3 the 36*i* split position was adopted opposed to the 6*c* position typically displayed by the palmierite structure. The assignment of the 36*i* position is common for $Ba_3M'M''O_{8.5}$ structures, and models the positional oxygen disorder in the palmierite layer [16,27]. Positional disorder of O2 is also shown by the large U_{iso} as previously reported for $Ba_3NbMoO_{8.5}$ [18]. The Ba1 fractional occupancy was refined to within ±1% of the full occupancy and was subsequently fixed at 1.0. The Ba2 occupancy was allowed to refine freely

resulting in an occupancy of 0.844(2). Refining the Ba2 occupancy resulted in an excellent Rietveld fit with the statistical parameters reducing significantly from χ^2 = 5.437, R_p = 2.58 %, R_{wp} = 2.08 % to χ^2 = 3.077, R_p = 1.99 %, R_{wp} = 1.49 % (Fig. 4, Fig. S2 and Table 1).

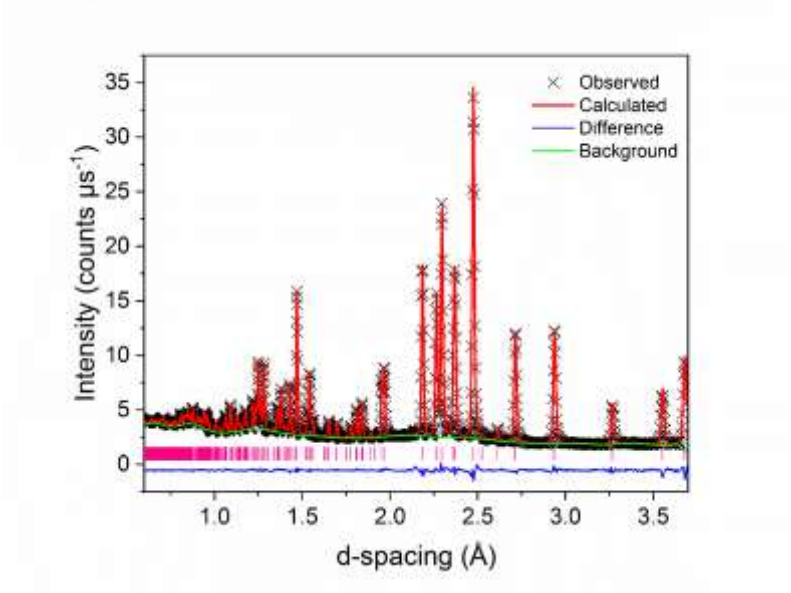

Figure 4. Fitted neutron diffraction histogram for $Ba_{3-x}VMoO_{8.5-x}$ with TOF neutron data from the 90° detector bank of the Polaris diffractometer. Black crosses show the observed data, red line the Rietveld fit, the blue line shows the difference between the observed and calculated patterns, the green line is the background function, and the pink vertical bars show the reflection positions.

Table 1. Refined atomic parameters from the Rietveld fit to the $R\bar{3}m$ *H* model from powder neutron diffraction data recorded on the Polaris diffractometer.

Atom	Site	*x*	*y*	*Z*	Fraction	$U_{11} = U_{22}$	U_{33}	U_{12}	U_{13}	U_{23}
Ba1	3*a*	0	0	0	1	0.0380(4)	0.0046(5)	0.0190(2)	0	0
Ba2	6*c*	0	0	0.20348(4)	0.844(2)	0.0423(4)	0.0210(5)	0.0211(2)	0	0
M1	6*c*	0	0	0.40086(5)	1	0.0155(3)	0.0249(7)	0.0077(2)	0	0
O1	18*h*	0.17299(4)	0.82701(4)	0.09967(2)	1	0.0256(2)	0.0285(3)	0.0215 (2)	0.0001 (1)	-0.0001 (1)
O2	9*e*	0.5	0	0	0.136(1)	0.052(2)*	-	-	-	-
O3	36*i*	0.0496(4)	0.0520(4)	0.32521(4)	0.149(1)	0.022(6)*	-	-	-	-

*U_{iso} (Å^2)

Data were refined in space group $R\bar{3}m$ *H* with χ^2 = 3.077, R_p = 1.99 %, R_{wp} = 1.49 %; refined unit cell parameters; *a* = *b* = 5.86982(5) Å, *c* = 21.3061(2) Å, *V* = 635.775(14) Å^3. U_{ij} (in Å^2) represent anisotropic displacement parameters. The M1 site is composed of 50% V and 50% Mo.

The results from the Rietveld refinement clearly show barium non-stoichiometry which is most likely due to barium volatilisation upon heating leading to a stoichiometry of 2.688(4). As a consequence, the sample is also found to be oxygen deficient which is clear upon refinement of the oxygen fractional occupancies resulting in an overall oxygen stoichiometry of 8.20(3). The O1 site is fully occupied while the O2 and O3 sites display partial occupancy. As a result, the stoichiometry of this phase is determined to be $Ba_{2.69}VMoO_{8.20.}$ The results from the Rietveld refinement show no significant correlation between either of the Ba2 or O2 displacement parameters and refined site occupancies. The bond valence sums (BVS) for the Ba cations were calculated by the *soft*BV program at 2.05(3) and 1.91(3) for Ba1 and Ba2 respectively. The results demonstrate favourable bonding environments for both Ba cations as the Ba non-stoichiometry is compensated for by the reduction in the oxygen fractional occupancy in the palmierite layer. The average BVS for V/Mo is 5.53(3) as expected for V^{5+} and Mo^{6+}. This corroborates that the oxidation state of vanadium is 5+ as previously reported for $Ba_3VWO_{8.5}$ [27].

Selected bond lengths and angles of $Ba_{3-x}VMoO_{8.5-x}$ compared with the other members of the $Ba_3M'M''O_{8.5}$ family can be seen in Tables S2 and S3 respectively. As is typical for the $Ba_3M'M''O_{8.5}$ family, $Ba_{3-x}VMoO_{8.5-x}$ displays three M1-O1 bonds of equal length and three equal O1-M1-O1 angles which forms an $M1(O1_3)$ unit that is found in both $M1(O1_3O2_3)$ octahedra and $M1(O1_3O3)$ tetrahedra [16,23,27]. $Ba_{3-x}VMoO_{8.5-x}$ displays the longest Ba2-O1, Ba2-O2 and Ba2-O3 bond lengths as a result of the Ba-deficiency. As the Ba2 site is not fully occupied in $Ba_{3-x}VMoO_{8.5-x}$ the oxygen atoms move closer to the V/Mo metal sites leading to longer Ba2-O bond lengths. In turn this results in shorter M1-O1 and M1-O3 bond lengths, compared to $Ba_3NbMoO_{8.5}$ [16]. The average M1-O1 bond length (1.7682(5) Å) is noticeably shorter and in turn the O1-M1-O1 angle (105.962(34) °) larger in $Ba_{3-x}VMoO_{8.5-x}$ compared with other $Ba_3M'M''O_{8.5}$ compounds. The shorter bond lengths are also potentially due to the presence of vanadyl bonds as previously reported for $Ba_3VWO_{8.5}$ [21,27,35].

The analysis of the minimum bounding ellipsoid, which can be described as the ellipsoid of the smallest volume containing all the atoms of a coordination polyhedron, was performed using the PIEFACE software package (Table S4) [31]. The distortion of a polyhedral can be mapped out by calculating σ(*R*), which is the standard deviation of the three principal ellipsoid's radii (Rx, Ry, and Rz). In $Ba_{3-x}VMoO_{8.5-x}$ the octahedral units display the highest σ(*R*) value (0.09430 Å) of the $Ba_3M'M''O_{8.5}$ family followed by $Ba_3NbMoO_{8.5}$ and $Ba_3VWO_{8.5}$ which have similar σ(*R*) (0.07612 Å and 0.0753 Å respectively) while $Ba_3NbWO_{8.5}$ presents the lowest σ(*R*) (0.04752 Å). In contrast, the distortion of the tetrahedral units exhibited by $Ba_{3-x}VMoO_{8.5-x}$ is notably smaller than the other $Ba_3M'M''O_{8.5}$ phases with σ(*R*) of 0.00144 Å compared with 0.02101 Å, 0.04821 Å and 0.04883 Å for $Ba_3NbWO_{8.5,}$ $Ba_3VWO_{8.5}$ and $Ba_3NbMoO_{8.5}$ respectively [6,27].

The ratio of tetrahedral to octahedral units varies greatly for the $Ba_3M'M''O_{8.5}$ phases with $Ba_{3-x}VMoO_{8.5-x}$ presenting the highest percentage of tetrahedra (~86.8%) in the average structure at room temperature, followed by $Ba_3VWO_{8.5}$ (~66.2%), then $Ba_3NbMoO_{8.5}$ (~49.9%) with $Ba_3NbWO_{8.5}$ displaying the lowest percentage (~13.1%) [20,23,27]. This ratio depends on the geometrical preference of the cations present, with V^{5+} and Mo^{6+} favouring tetrahedral geometry while Nb^{5+} and W^{6+} typically adopt octahedral geometry [21]. A recent study investigating the effect of pressure on $Ba_3NbMoO_{8.5}$ concluded that, as pressure is increased, the percentage of tetrahedra decreases, which results in greater distortion of the tetrahedral units [36]. On the contrary, in $Ba_{3-x}VMoO_{8.5-x}$ the geometry of the palmierite-like layer is predominantly tetrahedral resulting in a much-reduced distortion of the tetrahedral units. The occurrence of neighbouring octahedral and tetrahedral units in $Ba_3M'M''O_{8.5}$ is facilitated by local disruption of the oxygen sublattice [18]. In $Ba_{3-x}VMoO_{8.5-x}$ the concentration of octahedra is much reduced compared to other members of the family so that the probability of a tetrahedral unit to be neighbouring an octahedral unit is smaller and hence the tetrahedra are less distorted. In contrast the octahedral units are now more likely to be neighbouring a tetrahedral unit. In this case the O2 atom is displaced away from the O3 in the neighbouring tetrahedra, creating a distorted octahedron as evidenced by the larger $\sigma(R)$ and atomic displacement parameter of O2.

The octahedra are further distorted as a result of an out-of-centre displacement arising from the second-order Jahn-Teller (SOJT) distortion of the d^0 cations [16,18,37]. This level of distortion can be linked to the formal charge and ionic radius of the cations, with a higher charge and smaller radius contributing to greater levels of distortion [37]. Considering this, Mo^{6+} and V^{5+} can be described as strong distorters while Nb^{5+} and W^{6+} are moderate distorters [38]. $Ba_{3-x}VMoO_{8.5-x}$ contains both V^{5+} and Mo^{6+} and is therefore expected to display the most distorted average $M1O_6$ octahedra when compared with other $Ba_3M'M''O_{8.5}$ phases. The out of-centre displacement (D) of the metal cations can be examined in regard to their movement away from the O2/O3 sites and towards the O1-O1-O1 face of the $M1O_x$ unit [20]. The $M1O_6$ octahedra in $Ba_{3-x}VMoO_{8.5-x}$ exhibit the largest D of all $Ba_3M'M''O_{8.5}$ phases (D = 0.4179 Å, Table S4). As a consequence the M1-O2 bond length is the longest reported for a $Ba_3M'M''O_{8.5}$ structure as a result of both the SOJT and disorder of the O(2) site.

Bond-valence site energy (BVSE) calculations were performed to investigate the migration pathways of the oxide ion and determine the energy landscape in the average crystal structure of $Ba_{3-x}VMoO_{8.5-x}$. BVSE analysis produces results which are in relative agreement with more accurate density functional theory (DFT) calculations, at a fraction of the computational cost [32]. This approach has previously been highly successful in identifying conduction pathways and energetics of $Ba_3Nb_{3.9}V_{0.1}MoO_{8.5}$ and $Ba_3VWO_{8.5}$ [22,27]. The refined structural model of $Ba_{3-x}VMoO_{8.5-x}$ from neutron diffraction data was used to carry out these calculations using the *soft*BV programme. BVSE

landscapes of the interactions of a probe oxide ion are generated by the programme to determine connecting local minima, saddle points and relative energy barriers [32].

The migration of oxide ions along the palmierite layers of the average structure occurs via two saddle points with corresponding relative energy barriers. The first saddle point, S1, corresponds to the diffusion of oxide ions along the partially occupied O2/O3 sites (Fig. 5a). The relative energy barrier , E1 (Fig. 5c) is therefore associated with the occupation of the mobile oxygen crystallographic sites O2/O3 as reported for other $Ba_3M'M''O_{8.5}$ phases [22,27]. Greater occupation of the O3 site leads to a higher percentage of lower coordination environments which are more suited for diffusion of oxide ions throughout the structure resulting in a decrease of E1. The height of E1 for $Ba_{3-x}VMoO_{8.5-x}$ is considerably smaller than that of $Ba_3NbMoO_{8.5}$ because of the increased number of tetrahedra observed in $Ba_{3-x}VMoO_{8.5-x}$. This is consistent with the $Ba_3Nb_{1-x}V_xO_{8.5}$ series, which shows a decrease in the E1 energy barrier as the dopant level was increased due to a greater percentage of tetrahedral units [22].

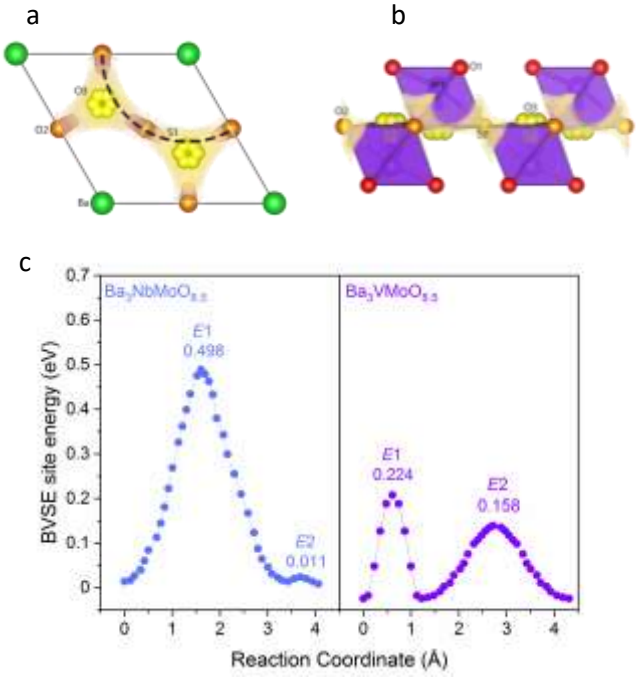

Figure 5. BVSE maps of $Ba_{3-x}VMoO_{8.5-x}$ displaying two-dimensional diffusion pathways along palmierite layers down the (a) *c*-axis and (b) *a*-axis. (c) BVSE models of migration barriers along the palmierite layers for $Ba_3NbMoO_{8.5}$ and $Ba_{3-x}VMoO_{8.5-x}$. Relative bond-valence energy barriers are displayed in eV.

The second saddle point, S2, is perpendicular to the undulating distribution of crystallographic oxygen sites (Fig. 5b). The E2 relative energy barrier (Fig. 5c), which is related to the S2 saddle point, describes

the energy required to allow for the relaxation of oxygen atoms during the migration of oxide ions between O2 and O3 sites with the relative height linked to the polyhedral distortion [22]. E2 is noticeably larger for $Ba_{3-x}VMoO_{8.5-x}$ than $Ba_3NbMoO_{8.5}$, which is indicative of the increase in octahedral distortion. Two-dimensional O2-O3 conduction pathways (on the *ab* plane) along the palmierite layers corresponding to the E1 and E2 energy barriers are observed and are expected to have the greatest contribution to the overall conductivity of $Ba_3M'M''O_{8.5}$. Further to the investigation of two-dimensional pathways and energy barriers for $Ba_3M'M''O_{8.5}$, *soft*BV can be utilised to calculate all pathway segments and study the connectivity for a given structure [33]. BVSE maps of the average structures of $Ba_3NbMoO_{8.5}$ and $Ba_3NbWO_{8.5}$ have indicated a degree of connectivity between adjacent O1-O2 and O1-O1 positions in $Ba_3NbMoO_{8.5}$ and $Ba_3NbWO_{8.5}$, suggesting the migration of oxide ions along the edges of $M1O_x$ and $M2O1_6$ polyhedral units. While the O1-O2 connectivity along the edge of the $M1O_x$ units is witnessed for $Ba_3VWO_{8.5}$ (relative energy barrier of 0.780 eV), the O1-O1 pathways are not present along the edges of the vacant octahedral units [27]. $Ba_{3-x}VMoO_{8.5-x}$ is isostructural with $Ba_3VWO_{8.5}$ where the O1-O2 connectivity is observed (with a relative energy barrier of 0.371 eV) but the O1-O1 pathway segment is also absent preventing long-range diffusion parallel to the *c*-axis thus corroborating the previous hypothesis that ordering of the cationic vacancies in the $Ba_3M'M''O_{8.5}$ structure prevents three-dimensional ionic transport [27]. The results from BVSE analysis suggest that oxide ion conductivity is present in $Ba_{3-x}VMoO_{8.5-x}$. However the presence of a larger energy barrier at S2 and reduced connectivity along *c* would suggest that the bulk ionic conductivity of $Ba_{3-x}VMoO_{8.5-x}$ is likely to be lower than that reported for the other $Ba_3M'M''O_{8.5}$ phases.

Summary

In summary, we have successfully synthesised and determined the crystal structure of the hexagonal perovskite derivative $Ba_{3-x}VMoO_{8.5-x}$. One important difference between $Ba_{3-x}VMoO_{8.5-x}$ and other members of the $Ba_3M'M''O_{8.5}$ family is that it is non-stoichiometric with a chemical formula $Ba_{2.69}VMoO_{8.20}$. It is likely that this barium and oxygen non-stoichiometry results in the poor stability of this phase upon heating above 300 °C in air or O_2. BVSE analysis shows that oxide ion conduction is likely in the *ab* plane. Synthesis of a stoichiometric sample is warranted to further investigate the electrical properties. This could potentially be achieved by adding excess $Ba(OH)_2$ or by substitution of a small amount of W^{6+} for Mo^{6+} as the $Ba_3VWO_{8.5}$ phase is stoichiometric.

Acknowledgements

We thank the UK Science and Technology Facilities Council (STFC) for provision of Xpress Access neutron beamtime at ISIS. This research was supported by the Leverhulme trust (RPG-2017-351 and

DS-2017-073). DNT, a Leverhulme Trust Doctoral Scholar, is part of the 15 PhD scholarships of the "Leverhulme Centre for Doctoral Training in Sustainable Production of Chemicals and Materials" at the University of Aberdeen (Scotland, United Kingdom). AG is supported by the Commonwealth Scholarship Commission.

Associated Content

Supporting information consists of table of crystallographic data and figures showing Rietveld refinement fits.

References

1 L. Malavasi, C. A. J. Fisher and M. S. Islam, Oxide-ion and proton conducting electrolyte materials for clean energy applications: structural and mechanistic features. *Chem. Soc. Rev.*, 2010, **39**, 4370–4387.

2 B. C. H. Steele and A. Heinzel, Materials for fuel-cell technologies. *Nature*, 2001, **414**, 345–352.

3 J. B. Goodenough, A. Manthiram, M. Paranthaman and Y. S. Zhen, Oxide ion electrolytes. *Mater. Sci. Eng. B*, 1992, **12**, 357–364.

4 A. Brisse, J. Schefold and M. Zahid, High temperature water electrolysis in solid oxide cells. *Int. J. Hydrogen Energy*, 2008, **33**, 5375–5382.

5 A. J. Jacobson, Materials for Solid Oxide Fuel Cells. *Chem. Mater.*, 2010, **22**, 660–674.

6 S. Fop, K. S. McCombie, E. J. Wildman, J. M. S. Skakle and A. C. Mclaughlin, Hexagonal perovskite derivatives: a new direction in the design of oxide ion conducting materials. *Chem. Commun.*, 2019, **55**, 2127–2137.

7 J. C. Boivin and G. Mairesse, Recent Material Developments in Fast Oxide Ion Conductors. *Chem. Mater.*, 1998, **10**, 2870–2888.

8 A. Navrotsky, Thermodynamics of solid electrolytes and related oxide ceramics based on the fluorite structure. *J. Mater. Chem.*, 2010, **20**, 10577–10587.

9 F. Goutenoire, O. Isnard, R. Retoux and P. Lacorre, Crystal Structure of $La_2Mo_2O_9$, a New Fast Oxide−Ion Conductor *Chem. Mater.*, 2000, **12**, 2575–2580.

10 E. Kendrick, M. S. Islam and P. R. Slater, Developing apatites for solid oxide fuel cells: insight into structural, transport and doping properties. *J. Mater. Chem.*, 2007, **17**, 3104–3111.

11 F. Abraham, J. C. Boivin, G. Mairesse and G. Nowogrocki, The bimevox series: A new family of high performances oxide ion conductors. *Solid State Ionics*, 1990, **40**–**41**, 934–937.

12 P. Majewski, M. Rozumek and F. Aldinger, Phase diagram studies in the systems La_2O_3–SrO–MgO–Ga_2O_3 at 1350–1400°C in air with emphasis on Sr and Mg substituted $LaGaO_3$. *J. Alloys Compd.*, 2001, **329**, 253–258.

13 M. Morales, J. J. Roa, J. Tartaj and M. Segarra, A review of doped lanthanum gallates as electrolytes for intermediate temperature solid oxides fuel cells: From materials processing to electrical and thermo-mechanical properties. *J. Eur. Ceram. Soc.*, 2016, **36**, 1–16.

14 M. Li, M. J. Pietrowski, R. A. De Souza, H. Zhang, I. M. Reaney, S. N. Cook, J. A. Kilner and D. C. Sinclair, A family of oxide ion conductors based on the ferroelectric perovskite $Na_{0.5}Bi_{0.5}TiO_3$ *Nat. Mater.*, 2014, **13**, 31–35.

15 F. Yang, M. Li, L. Li, P. Wu, E. Pradal-Velázque and D. C. Sinclair, Optimisation of oxide-ion conductivity in acceptor-doped $Na_{0.5}Bi_{0.5}TiO_3$ perovskite: approaching the limit? *J. Mater.*

Chem. A, 2017, **5**, 21658–21662.

16 S. Fop, J. M. S. Skakle, A. C. McLaughlin, P. A. Connor, J. T. S. Irvine, R. I. Smith and E. J. Wildman, Oxide ion conductivity in the hexagonal perovskite derivative $Ba_3MoNbO_{8.5}$. *J. Am. Chem. Soc.*, 2016, **138**, 16764–16769.

17 J. Darriet and M. A. Subramanian, Structural relationships between compounds based on the stacking of mixed layers related to hexagonal perovskite-type structures. *J. Mater. Chem.*, 1995, **5**, 543–552.

18 J. E. Auckett, K. L. Milton and I. R. Evans, Cation Distributions and Anion Disorder in $Ba_3NbMO_{8.5}$ (M = Mo, W) Materials: Implications for Oxide Ion Conductivity. *Chem. Mater.*, 2019, **31**, 1715–1719.

19 M. S. Chambers, K. S. Mccombie, J. E. Auckett, A. C. Mclaughlin, J. T. S. Irvine, P. A. Chater, J. S. O. Evans and I. R. Evans, Hexagonal perovskite related oxide ion conductor $Ba_3NbMoO_{8.5}$: phase transition, temperature evolution of the local structure and properties. *J. Mater. Chem. A*, 2019, **7**, 25503–25510.

20 S. Fop, E. J. Wildman, J. T. S. Irvine, P. A. Connor, J. M. S. Skakle, C. Ritter and A. C. McLaughlin, Investigation of the Relationship between the Structure and Conductivity of the Novel Oxide Ionic Conductor $Ba_3MoNbO_{8.5}$. *Chem. Mater.*, 2017, **29**, 4146–4152.

21 D. Waroquiers, X. Gonze, G. M. Rignanese, C. Welker-Nieuwoudt, F. Rosowski, M. Göbel, S. Schenk, P. Degelmann, R. André, R. Glaum and G. Hautier, Statistical Analysis of Coordination Environments in Oxides. *Chem. Mater.*, 2017, **29**, 8346–8360.

22 S. Fop, K. McCombie, R. I. Smith and A. C. McLaughlin, Enhanced Oxygen Ion Conductivity and Mechanistic Understanding in $Ba_3Nb_{1-x}V_xMoO_{8.5}$. *Chem. Mater.*, 2020, **32**, 4724–4733.

23 K. S. McCombie, E. J. Wildman, S. Fop, R. I. Smith, J. M. S. Skakle and A. C. McLaughlin, The crystal structure and electrical properties of the oxide ion conductor $Ba_3WNbO_{8.5}$. *J. Mater. Chem. A*, 2018, **6**, 5290–5295.

24 A. Bernasconi, C. Tealdi and L. Malavasi, High-Temperature Structural Evolution in the $Ba_3Mo_{(1-x)}W_xNbO_{8.5}$ System and Correlation with Ionic Transport Properties. *Inorg. Chem.*, 2018, **57**, 6746–6752.

25 M. Coduri, A. Bernasconi, H. E. Fischer and L. Malavasi, The $Ba_3Mo_{1-x}W_xNbO_{8.5}$ ion conductors: insights into local coordination from X-ray and neutron total scattering. *J. Mater. Chem. A*, 2020, **8**, 21227–21240.

26 S. Fop, K. S. Mccombie, E. J. Wildman, J. M. S. Skakle, J. T. S. Irvine, P. A. Connor, C. Savaniu, C. Ritter and A. C. Mclaughlin, High oxide ion and proton conductivity in a disordered hexagonal perovskite. *Nat. Mater.*, 2020, **19**, 752–757.

27 A. Gilane, S. Fop, F. Sher, R. Smith and A. C. Mclaughlin, The relationship between oxide-ion conductivity and cation vacancy order in the hybrid hexagonal perovskite $Ba_3VWO_{8.5}$. *J. Mater. Chem. A*, 2020, **8**, 16506–16514.

28 R. B. Von Dreele and A. C. Larson, General structure analysis system (GSAS); Report LAUR 86−748; Los Alamos National Laboratory, 1994.

29 B. H. Toby, EXPGUI, a graphical user interface for GSAS. *J. Appl. Crystallogr.*, 2001, **34**, 210–213.

30 V. F. Sears, Neutron scattering lengths and cross sections. *Neutron News*, 1992, **3**, 26–37.

31 J. Cumby and J. P. Attfield, Ellipsoidal analysis of coordination polyhedra. *Nat. Commun.*, 2017, **8**, 14235.

32 H. Chen, L. L. Wong and S. Adams, SoftBV – a software tool for screening the materials genome of inorganic fast ion conductors. *Acta Crystallogr. Sect. B Struct. Sci. Cryst. Eng. Mater.*, 2019, **75**, 18–33.

33 H. Chen and S. Adams, Bond softness sensitive bond-valence parameters for crystal structure plausibility tests. *IUCrJ*, 2017, **4**, 614–625.

34 K. Momma and F. Izumi, VESTA 3 for three-dimensional visualization of crystal, volumetric and morphology data. *J. Appl. Crystallogr.*, 2011, **44**, 1272–1276.

35 M. Schindler, F. C. Hawthorne and W. H. Baur, Crystal Chemical Aspects of Vanadium: Polyhedral Geometries, Characteristic Bond Valences, and Polymerization of (VO_n) Polyhedra. *Chem. Mater.*, 2000, **12**, 1248–1259.

36 B. Sherwood, C. J. Ridley, C. L. Bull, S. Fop, J. Skakle, A. C. Mclaughlin and E. Wildman, A pressure induced reversal to the 9R perovskite in $Ba_3MoNbO_{8.5}$. *J. Mater. Chem. A*, 2021, **9**, 6567–6574.

37 M. Kunz and I. David Brown, Out-of-Center Distortions around Octahedrally Coordinated d^0 Transition Metals. *J. Solid State Chem.*, 1995, **115**, 395–406.

38 K. M. Ok, P. S. Halasyamani, D. Casanova, M. Llunell, P. Alemany and S. Alvarez, Distortions in Octahedrally Coordinated d^0 Transition Metal Oxides: A Continuous Symmetry Measures Approach. *Chem. Mater.*, 2006, **18**, 3176–3183.

For Table of Contents only

The crystal structure of the hexagonal perovskite derivative Ba3-xVMoO8.5-x which has ordered cation vacancies. Ba3-xVMoO8.5-x is unstable in air above 400 °C, which precludes measurement of the electrical properties. However, bond-valence site energy (BVSE) calculations strongly suggest that oxide ion conductivity is present in Ba3-xVMoO8.5-x .